OCT-elastography-based optical biopsy for breast cancer delineation and express assessment of morphological/molecular subtypes

EKATERINA V. GUBARKOVA,[1,*] ALEXANDER A. SOVETSKY,[2] VLADIMIR YU. ZAITSEV,[2] ALEXANDER L. MATVEYEV,[2] DMITRY A. VORONTSOV,[3] MARINA A. SIROTKINA,[1] LEV A. MATVEEV,[2] ANTON A. PLEKHANOV,[1] NADEZHDA P. PAVLOVA,[1] SERGEI S. KUZNETSOV,[1] ALEXEY YU. VORONTSOV,[3] ELENA V. ZAGAYNOVA,[1] AND NATALIA D. GLADKOVA[1]

[1]*Privolzhsky Research Medical University, Nizhny Novgorod, Russia*
[2]*Institute of Applied Physics RAS, Nizhny Novgorod, Russia*
[3]*Nizhny Novgorod Regional Oncologic Hospital, Nizhny Novgorod, Russia*
*kgybarkova@mail.ru

Abstract: Application of compressional optical coherence elastography (OCE) for delineation of tumor and peri-tumoral tissue with simultaneous assessment of morphological/molecular subtypes of breast cancer is reported. The approach is based on the ability of OCE to quantitatively visualize stiffness of studied samples and then to perform a kind of OCE-based biopsy by analyzing elastographic B-scans that have sizes ~several millimeters similarly to bioptates used for "gold-standard" histological examinations. The method relies on identification of several main tissue constituents differing in their stiffness in the OCE scans. Initially the specific stiffness ranges for the analyzed tissue components (adipose tissue, fibrous and hyalinized tumor stroma, lymphocytic infiltrate and agglomerates of tumor cells) are determined via comparison of OCE and morphological/molecular data. Then assessment of non-tumor/tumor regions and tumor subtypes is made based on percentage of pixels with different characteristic stiffness ("stiffness spectrum") in the OCE image, also taking into account spatial localization of different-stiffness regions. Examples of high contrast among benign (or non-invasive) and several subtypes of invasive breast tumors in terms of their stiffness spectra are given.

1. Introduction

Breast cancer is the most commonly diagnosed cancer and second leading cause of cancer death among women [1]. Breast cancer is a multi-type disease, exhibiting broad diversity of clinical, morphological, and molecular characteristics between tumors and even within a single tumor [2,3]. Deeper insight in breast cancer variability is important not only for diagnostic procedures, but also for the choice of treatment tactics. Breast cancer types is conventionally subdivided in non-invasive (Ductal cancer *in situ* - DCIS) and several invasive types - Luminal A, Luminal B, HER2-positive (not-luminal), and basal-like (triple negative) subtypes [4]. These groups have significantly different implications for treatment tactics and prognosis. Intraoperative assessment of the surgical margin (clean margin) can reduce the proportion of recurrence [4–6]. For more accurate detection of tumor margin, it is important take into account morphological and molecular breast cancer characteristics, which may differently manifest themselves for different diagnostic methods. However, the existing nondestructive intraoperative imaging methods for determining negative margins are limited and are considered insufficient. Modern imaging methods of breast cancer, such as

ultrasound, X-ray computed tomography, positron emission tomography and magnetic resonance imaging can determine the size of a tumor or lymph node, the general morphological information [7], but the low resolution does not allow to detect lesion less than a few mm and determine the negative surgical margin.

Recent progress in biophotonics methods gives reasons to expect that, for such applications, much more promising can be an optical high-resolution technology, approaching the histopathology level in detaling and operating in nearly-real time to rapidly assess the microscopic status of lumpectomy margins. Optical coherence tomography (OCT) opens interesting prospects in solving this challenging problem [8,9]. For example, *ex vivo* studies show improvements of tumor/healthy tissue contrast (based on collagen detection) using a polarization-sensitive OCT (PS-OCT) [10,11] in comparison with conventional structural OCT imaging.

Significant attention in recent years has been paid to elastic properties of tissues [12] which are known to be related to their function and structure that can be changed due to pathology development, as well as in the course of treatment. Although conventional structural OCT images do not directly visualize information about the tissue stiffness, such information can be obtained by comparing OCT images of the tissue in a reference and deformed states, which is the basic principle of compression (or compressional) variant of Optical Coherence Elastography (OCE) [13–17]. Attention to the problem of determining tissue stiffness (elastographic mapping) by OCE methods has been increasing in recent years. Application of compressional OCE to characterize mechanical properties of tissues was demonstrated for *ex vivo* human breast cancer specimens [17]. New possibilities opened for intraoperative assessment of the breast cancer borders by means of OCE were demonstrated in a recent paper [18]. The potential of the method was shown to provide a contrast between malignant and normal tissues of mammary gland. In addition, it was found that OCE-based imaging of spatial micro-scale heterogeneity of tissue stiffness simplifies assessment of human breast cancer [19]. However, benign breast lesions may also have a heterogeneous distribution of elastic properties due to the presence of various structures in the breast tissue, which may confound the diagnosis of a clear breast cancer margin. This indicates the necessity of getting a deeper insight in this intrinsic tissue heterogeneity. Besides, there is a lack of possibilities for express diagnosis of especially aggressive tumors (e.g. triple-negative cancer), for which special types of therapy and surgery (mostly mastectomy) may be required to prevent the disease recurrence. So, despite the recent technological advances [20], there remains a critical need to improve means for rapid detection, differentiation, and diagnosis of breast tumor tissue, including differentiation of morphological and molecular features of breast cancer, comparable with the information value of histopathological examination.

In this context, interesting possibilities might be suggested by emerging OCE techniques. By now, despite the above-mentioned progress in OCE, methods for interpretation of OCE images allowing for express assessment of breast cancer subtypes (including both morphological and molecular features) have not been directly studied and evaluated.

Here, using analysis of OCE-data for excised samples of several types of malignant breast tumors, as well as breast tissue in normal and pre-cancer states, we demonstrate promising capabilities of OCE not only for conventionally discussed delineation of non-tumor/tumor regions, but also for revealing qualitative and quantitative differences among several breast cancer subtypes. This concerns prospects of the proposed OCE-based approach for assessing morphology (i.e., presence of fibrous and hyalinized stroma, lymphohistiocytic inflammatory infiltrate, agglomerates of tumor cells), the degree of malignancy of tumors and even for discrimination of cancer subtypes with different molecular portraits.

Similarly, to typical histological studies of bioptates, the proposed OCE assessment is based on analysis of fairly local (~a few millimeters in size) OCE B-scans. Thus, the method can be viewed as a kind of optical biopsy based on analysis of percentages of pixels corresponding to several specific ranges of the Young modulus within the visualized area. By

analogy with the term "mass-spectroscopy", the assessment based on stiffness ranges for the heterogenous-tissue constituents can be called "elasto-spectroscopy" (and should not be confused with ultrasonic spectroscopy essentially based on frequency-dependent data). In some cases (e.g., in the case of ductal breast cancers with predominant localization of tumor-cells inside and near ducts), additional information about spatial heterogeneity of the stiffness distribution is also used. The proposed OCE-based examination does not require any special procedures (like fixation, dehydration, staining, etc.) typical for preparation of histological samples, so that the OCE assessment can be performed on a few-minute intervals and, consequently, has a potential to be realized intra-operatively. In what follows we demonstrate that the information value of such express OCE-based diagnostics can be comparable with histopathological examination of bioptates.

2. Materials and methods

2.1. Patient selection and data collection

The present study was approved by the Institutional Review Board of the Privolzhsky Medical Research University (Nizhny Novgorod, Russia). All of the patients included in the study provided written informed consent. The research was carried out on 56 specimens of freshly excised breast tissue acquired from 33 patients (mean age: 63 years; age range 30-88 years) undergoing mastectomy (Fig. 1(a)). During resection, tumorous tissue specimens were taken from different parts of the tumor - in the center and peritumoral (normal) area. All specimens were studied within 1-2 hours after resection. Histopathology results were obtained for all patients and were classified into benign and malignant breast lesions (see section 2.5).

2.2. Multimodal OCT setup

This study used a custom-made common path spectral domain multimodal OCT system with a central wavelength of 1310 nm and spectral width of 100 nm, resulting in axial resolution of 10 μm, lateral resolution is 15 μm, scanning depth of 2 mm in air, scanning speed of 20000 A-scans per second. The scanning head allowed for performing 2D lateral scanning either in B-M-mode (with the typical B-scan size 256x256 pixels) for subsequent elastographic analysis or to obtain structural 3D scans [21]. The system was also capable to obtain in real time polarization-sensitive images (using co- and cross-polarized backscattered light) of the tissue structure, which can be used for evaluating the state of connective tissue component based on the cross-polarization OCT (CP OCT).

2.3. CP OCT imaging

The CP OCT images were constructed in two virtual channels, one of which was co-polarized with the incident polarization (co-polarization channel) and the other one was orthogonal (cross-polarization channel) to the incident polarization, respectively [22,23]. CP OCT is aimed to get the information, contained in the cross-polarization channel, which allows one to visualize birefringence of the tissue from optically anisotropic structures, as well as coherent cross-polarization backscattering on non-spherical particles and fibrous structures and particles with dimensions much larger than the wavelength. In the process of 3D scanning, sets of several tens of B-scans (of which 3D image was composed) were obtained in co- and cross- polarization within the area of 2.4x2.4 mm^2.

2.4. OCE imaging

A variant of compressional OCE described in [15,24–26] was used to visualize local inter-frame strains in the tissue induced by the tissue deformation. For estimating strains, local gradients of inter-frame phase-variations were calculated using an improved version of the phase-sensitive monitoring of scatterer displacements in the tissue and a robust vector method [16,25] for estimating the gradients.

For quantification of tissue stiffness in compressional OCE, a calibration (silicone) layer with preliminary calibrated stiffness was used. The silicone with the Young's modulus in the range 50-100 kPa was found to be the most suitable for studying breast tissue stiffness variations in the range from 20 kPa to 1000 kPa or even greater. The reference silicone layer with a known stiffness (used as stress sensor) was placed on the tissue surface, the probe was slightly pressed onto the studied tissue (Fig. 1(b)), and the resultant strain distribution under the OCT probe was reconstructed in a uniform manner in both silicone and tissue (which is somewhat different from the usage of reference silicone layers in such realizations of compressional OCE as described in [14]). Schematic Fig. 1(c) shows a typical inter-B-scan phase variation in the studied tissue overlaid by the reference silicone layer that is clearly seen in the structural B-scan OCT image (Fig. 1(d)). The interframe strains were estimated using the developed robust vector method [25]. In this method, for finding strains, the axial gradients of inter-frame phase variations are found by operating with the complex-valued OCT signals as vectors in the complex plane. This ensures the possibility of amplitude weighting with simultaneous suppression of especially strong phase errors ~π rad [25]. Further increase in the signal-to-noise ratio was obtained by averaging the vectors over a processing window (fairly small in comparison with the entire scan). In the considered examples the windows of 16x16 pixels were used (see the small rectangle in the silicone in Fig. 1(e)). Thus, in the resultant 2D strain maps, the resolution (on the order of 1/2 of the averaging-window size) was about 4 times lower than in the initial OCT images, i.e., ~40-50 µm in both directions.
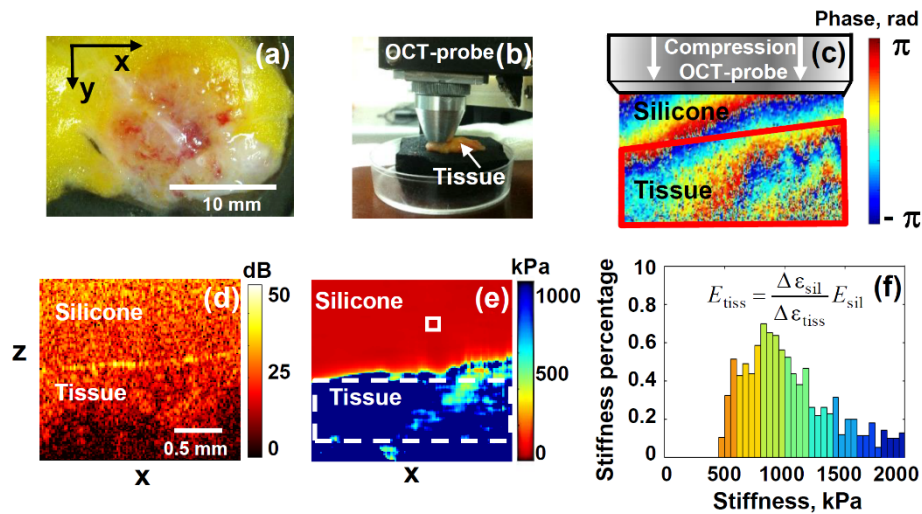

Fig. 1. Elucidation of experimental OCE procedures. Panel (a) is the photo of a typical breast-tissue sample; (b) shows the OCT probe pressing onto the studied sample; (c) is a color-coded map of inter-frame phase variation; (d) structural OCT B-scan of cancerous tissue under reference silicone; (e) is the reconstructed OCE image obtained for the pre-selected strain level in the silicone (and, thus, standardized pressure applied to the tissue); (f) is a histogram showing the normalized stiffness spectrum (percentage of pixels with different Young modulus) in the tissue within the chosen ROI window shown by the dashed rectangle in the tissue in panel (e). The small rectangle in panel (e) in the upper silicone layer shows the area size, over which the phase-variation gradient was averaged for estimating local strains.

The silicone-tissue sandwich was subjected to manually-operated approximately monotonic compression during which a series of 200-400 B-scans was acquired covering the strain range ~several per cent in the silicone. The interframe strains for each pair of B-scans in the acquired sequence were used to obtain cumulative strains in the silicone and tissue (see details in [24,25]). For the pre-calibrated silicone, its strain defines the stress exerted onto the

tissue. Thus, in such a way spatially resolved stress-strain dependence was obtained for the studied tissue sample. The sought Young modulus of the tissue corresponds to the slope of this dependence. The modulus was estimated as the ratio of the stress and strain increments in a chosen standard stress range exerted by the reference silicone layer onto the studied tissue.

This standardization is important since our preliminary studies of breast-cancer samples in agreement with previous data [27] indicated that the stress-strain relationship for such tissues may exhibit pronounced nonlinearity [16], so that for apparently very moderate straining (within a few per cent only), the Young modulus may vary several times. This fact should be taken into account when comparing different data sets. Therefore, to ensure the possibility of meaningful comparison between samples from different patients obtained in different days and/or using different calibration layers, the Young modulus was estimated for the same pre-selected pressure created within the calibration layer. To obtain the chosen standard pressure range for every lateral position, the corresponding range of strain in the pre-calibrated silicone was automatically chosen by taking the respective range of B-scan numbers from the entire record. This method gave the possibility to quantitatively compare the Young modulus even for samples with different uneven thickness and potentially strongly variable stiffness over the frame. For the quantitative estimates presented below, we used the pressure range from 3 kPa to 5 kPa centered at 4 kPa. Reproducibility of such measurements, including the usage of calibration layers with different stiffness was verified in a separate series of experiments [28]. The so-obtained stiffness B-scans, were represented as color-coded maps for the Young's modulus (kPa), usually in the range from several kPa to 1000-2000 kPa as illustrated in Fig. 1(e).

The next step was to obtain and analyze the "stiffness spectra" for the samples, i.e. histograms showing percentages of pixels with different stiffness within a chosen region of interest (ROI) (see an example of such a histogram in Fig. 1(f)). A typical ROI window in the tissue, over which the stiffness histograms were found, is shown in the OCE map (Fig. 1(e)) by the dashed-line rectangle. For the fairly limited number (n = 56) of the studied breast-tissue samples, the ROI-windows in OCE images were selected manually (the positions/orientation of B-scans being preliminary chosen by visual examination of the samples).

Specifically, the windows were chosen in the middle part of the tissue image in the OCE scans, excluding noisy regions of too weak signals near the image bottom and layers too close to the tissue-silicone interface to avoid overlapping of the window with the silicone. The typical size of ROIs was 30 × 120 pixels (with pixel size ~4 microns in both directions) as shown in Figs. 2 and 3 below (see the dashed-line rectangles in the OCE images). The histograms were normalized to 100% over the total ROI area, so that the bin heights gave percentage of pixels corresponding to particular ranges of stiffness. The normalization ensures that the stiffness spectra do not strongly vary for different sizes of the ROI windows.

Certainly, for meaningful interpretation of the studied heterogeneous samples corresponding to a particular lesion type, the chosen window should cover a representative region containing numerous characteristic structural heterogeneities. It has been empirically found that for the breast-tissue samples, to satisfy this requirement lateral size of ROI windows ~0.5-3 mm is sufficient and can be varied in such a range without strong influence on the estimated stiffness spectra due to normalization (in what follows, we consider the corresponding examples). When a transition between different tissue types is present over the entire OCE scan (as in Fig. 5 below), this is usually well visible. In such a case, smaller windows could be chosen to characterize the stiffness spectrum for these different sub-regions of the image.

In what follows we show that the so-obtained normalized histograms (stiffness spectra) demonstrate strong differences among various types of studied lesions, which opens prospects for developing express procedures of OCE-based optical biopsy for differentiation of breast cancer subtypes and for assessing the negative surgical margin of resection.

2.5. Histopathology

After the OCT-based imaging, the scanning area was marked on the specimen with histological ink for easier correlation with histology. Then, the specimens were fixed in 10% formalin for 24 hours and were transferred to 70% ethanol and then paraffined for histological study. The paraffined specimen blocks were sliced through the marked area to match the plane of histological sections with the OCT B-scan position.

To determine the disease type and collagen content, staining of the histological slides with hematoxylin and eosin (H&E) and Van-Gieson's was performed. The histological slices were prepared using a Leica RM 2245 Rotary Microtome, described by a morphologist and photographed in transmitted light with a Leica DM2500 DFC (Leica Microsystems, Germany) microscope, equipped with a digital camera. The revealed histological types of breast tissue include: peritumoral (normal) breast tissue (number of samples n = 10), fibroadenoma (n = 7), ductal carcinoma *in situ* (DCIS) (n = 5) and invasive ductal carcinoma (IDC) (n = 34).

Next, molecular subtypes (hormone status) of breast cancer were determined based on the results of immunohistochemistry (IHC) assessment of estrogen receptor (ER), progesterone receptor (PR), Her2/neu and antigen Ki-67 expression. All IDC were divided into 5 molecular subtypes: Luminal A (ER + , PR + , Her2/neu - negative, Ki-67 <15) (n = 5), Luminal B (ER +, PR + , Her2/neu-, Ki-67> 15%) (n = 11), Luminal B (ER + , PR + , Her2/neu + , Ki-67> 15%) (n = 8), non-luminal (Her2/neo-enriched) (n = 5) and triple-negative (ER-, PR-, He2/neu - negative, Ki-67> 15%) (n = 5) breast cancers. Discrimination of morphological/molecular IDC subtypes is important for accurate disease prognosis and optimization of individual therapy options.

The results of the histopathology were compared with OCT-based findings. When performing such comparison/matching, one should bear in mind that even neighboring histological slices demonstrate noticeable variations in the visualized morphological tissue structure. Clear illustrations of this statement can be seen in Fig. 2, where the differently stained pairs of neighboring slices Figs. 2(e) and 2(i), as well as Figs. 2(g) and 2(k) are separated not greater than by tens of microns and are perfectly parallel. Despite the topological similarity, the mutual positions and geometrical sizes of the structural components (ducts, adipose-tissue layers) differ very pronouncedly even for these neighboring slices. However, for compared OCE scans and histological images, the uncertainty of matching evidently may be significantly greater than the distance between neighboring histological slices. Furthermore, the applied compression noticeably deforms the sample during the OCE examination and then the shape of the unloaded sample is additionally distorted during procedures of its preparation for histological examinations (fixation in formalin, de-hydration, paraffining, etc.) This important remark should be taken into account when comparing OCE and histological images: only larger (~hundreds of microns and greater) regions/components can be reasonably matched and compared on this scale, whereas smaller features (~tens of microns) may look significantly stronger distorted/displaced than for neighboring histological slices.

2.6 Statistical processing

The variable for statistical inter-group comparison was the average Young's modulus (E_{mean}) calculated from OCE images. The multiple comparisons with the Bonferroni correction were used, to compare normal breast tissue to benign and malignant breast cancers. All results are expressed as mean ± standard deviations (± SD) (see Fig. 6). In all cases, the differences were thus considered statistically significant when $p < 0.05$. The statistical data processing was done in Statistica 10.0 set (StatSoft, Inc., USA).

3. Results

3.1. Qualitative processing of the OCE images

In this section, we first qualitatively discuss main features of the OCT-based data, starting from conventional structural images complemented by polarization-sensitive ones, with the main focus on OCE imaging of stiffness properties that show the most clear differences between various tissue types/states. It is known that breast tumor tissue is usually very heterogeneous, which complicates reliable detection of infiltrated cancer in fibroadipose tissue. When studying the OCE-based features of different samples we were focused not only on identifying breast cancer in comparison with normal mammary gland tissue, but also on the possibility to differentiate morphological/molecular tumor subtypes, from which the intraoperative margin assessment, prognosis and treatment tactics may essentially depend.

We begin from consideration of complementary structural (including cross-polarization ones) OCT images, OCT-based elastographic maps of stiffness and corresponding histological images to reveal specific stiffness features for the breast tissue in the normal state and several types/stages of cancer development. We recall once again that when comparing different-type images it should be taken into account that shape of the samples after OCT examination was noticeably affected by procedures of fixation and dehydration for histological studies. Slight difference in the slice positions (even ~tens of microns as for histological slices with different staining as in Figs. 2(e) and 2(i)) also affects the geometry of the tissue structural components.

Figure 2 (most-left column) shows that normal breast tissue is fairly heterogeneous as is clear from histological slices, in which the terminal duct lobular units (TDLUs), adipose and fibrous tissue are visible. These different components exhibit slightly different scattering strength in co- and cross-polarized structural OCT images, but without strong suppression of the cross-polarized signal, which is known to be typical for regions of tumor cells. The corresponding OCE image (Fig. 2(m)) visualizes increased stiffness in the region of the lobular structures and lower stiffness in the surrounded soft fibrous and especially adipose tissue of the mammary gland. The histogram of stiffness (i.e., stiffness spectrum normalized to 100% over the region shown by the dashed rectangle in Fig. 2(q)) shows that over 60% of the OCE-image area has Young modulus in the range 0-100 kPa.

The 2nd column in Fig. 2 corresponds to fibroadenoma (not yet malignant, but already abnormal tissue) characterized by comparable OCT signal in co- and cross-polarization channels (Fig. 2 (b)). This is due to the presence of large fibrous collagen fibers having a dense structure (fibrous stroma, see histological images Figs. 2(f) and 2(j)). Fibroadenoma is characterized by an increase in stiffness (Fig. 2(n)) in comparison with normal breast tissue and well-localized areas with an increased elastic modulus in the area of atypical ductal hyperplasia (ADH) indicated by arrow in Fig. 2(n).

The 3rd and 4th columns in Fig. 2 show breast specimen with DCIS (yet non-invasive) and invasive ductal (Luminal A) carcinoma (IDC), having lower grade of invasiveness in comparison with other more aggressive invasive types (see Fig. 3). In the structural OCT images, the most informative are cross-polarization panels showing both regions with fairly high cross-polarization backscattering and (corresponding to the presence of connective tissue with anisotropic fibrous structure similar in scattering properties to normal tissue and fibroadenoma) and regions with reduced cross-polarization signal (where the tissue structure is more isotropic due to appearance of tumor cells), see Figs. 2(c) and 2(d)). However, regions with reduced cross-polarization scattering are also present in panels (a) for norm and (b) for fibroadenoma, so that there is no pronounced contrast between benign and malignant states even in polarization-sensitive OCT scans.

The situation is strongly different for OCE images (4th row in Fig. 2). The OCE images very clearly show the cross sections of the ducts filled with tumor cells for DCIS and Luminal A breast cancer as high-contrast zones with strongly increased stiffness (Figs. 2(o) and 2(p)),

which well agree with the histological images shown in 2nd and 3d rows in Fig. 2. Even for yet benign fibroadenoma, the regions of hyperplasia visualized in histological images and characterized by increased cell density in the ducts can also be clearly seen in OCE images (Fig. 2(n)). However, for hyperplasia (benign fibroadenoma) the increase in stiffness is lower than for DCIS and Luminal A breast cancers.
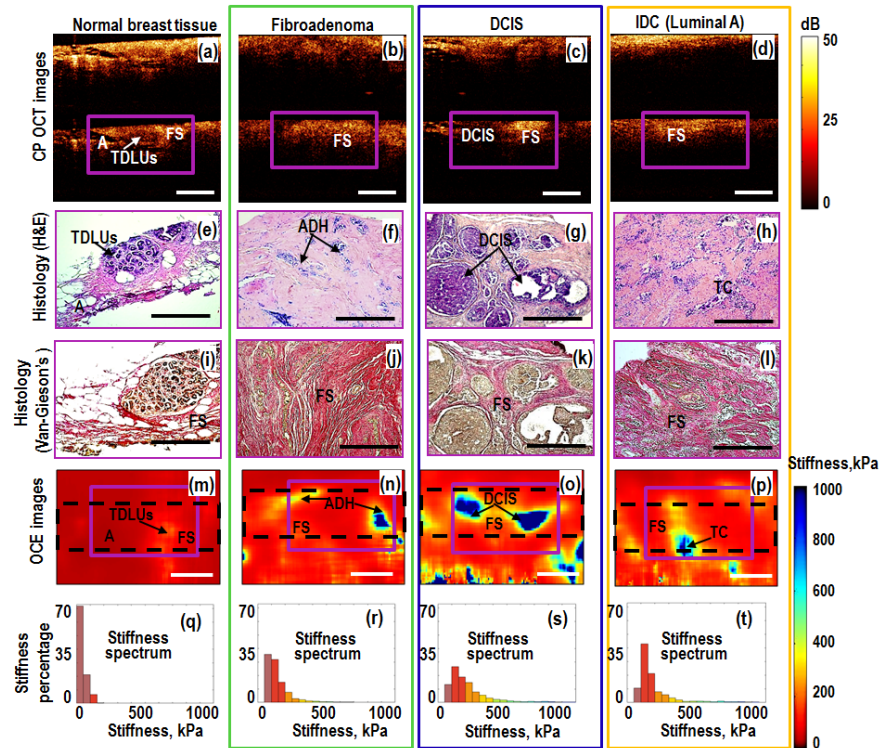

Fig. 2. Left-to-right columns present comparative OCT-based and histological results for: non-tumorous (normal) breast tissue, benign fibroadenoma (green box), non-invasive (blue box) and invasive (orange box) ductal breast carcinomas. Magenta-color (solid line) rectangles in the CP OCT and OCE images indicate the areas covered by respective histologic sections. The black dashed-line rectangles in the OCE images indicate the tissue areas, over which histograms of normalized stiffness spectrum were calculated. Letters in the images show areas of normal breast terminal duct lobular units (TDLUs); fibrous stroma (FS); adipose tissue (A), atypical ductal hyperplasia (ADH), ductal carcinoma *in situ* (DCIS), invasive ductal carcinoma (IDC) and agglomerates of tumor cells (TC). Scale bars correspond to 0.5 mm in all panels. Unlike Fig. 1(e) the upper silicone layer is not shown in the OCE images.

In the quantified form the above-mentioned features of stiffness distribution can be seen in the histograms (Figs. 2(q)-2(t)) that show the percentage of pixels with different stiffness for the normal breast tissue, fibroadenoma, DCIS and Luminal A breast cancer over the OCE-image regions shown in Figs. 2(m)-2(p), respectively. These histograms clearly demonstrate significant shift in stiffness distribution from the lowest values below 100 kPa (typical of the normal tissue) towards several times higher values in the case of fibroadenoma (with almost complete disappearance of small values <100 kPa). For the non-invasive DCIS and invasive Luminal A breast cancers, the fraction of stiffer cells is even higher. However, the next in the histological grade, invasive Luminal A breast cancer shows somewhat lower percentage of the most stiff fraction. This OCE-based observation well agrees with the histological images that demonstrate that, in comparison with localized stiff agglomerates of tumor cells inside ducts for DCIS, their concentration decreases when they penetrate from ducts into surrounding stromal tissue for Luminal A breast cancer. This results in some reduction in

percentage of the most stiff component in OCE scans. In more detail the proportions of different-stiffness components are discussed below.

The next Fig. 3 shows four representative examples of highly malignant, IDC with different morphological structure and molecular status with higher grades than in Fig. 2. Again in the polarization-sensitive structural OCT there are no pronounced differences between these subtypes and those in Fig. 2, although in regions of increased concentration of tumors cells the cross-polarization scattering is reduced. The OCE images again are the most informative. The difference between the OCE-scans for normal tissue and low-grade lesions in Fig. 2 and high-grade invasive tumors in Fig. 3 is striking. The high-grade invasive tumors demonstrate strongly increased proportion of stiff tumor cells over the scans and disappearance of highly localized regions of tumor cells embedded into surrounding much softer stromal tissue (compare Figs. 3(m)-3(p) with Figs. 2(o) and 2(p) for DCIS and Luminal A breast cancer. The histograms (Figs. 3(q)-3(t)) show clearly dominating and ever increasing percentage of stiff regions. In agreement with the histological slices, the OCE images clearly demonstrate ever diminishing proportion of the stromal component in the tumor tissue.
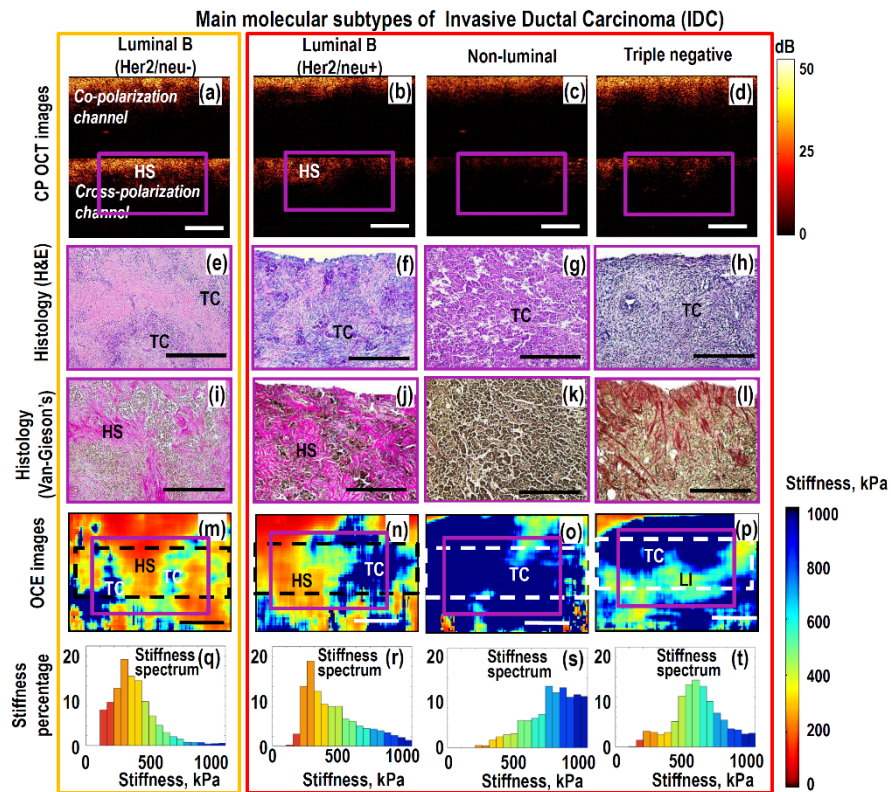

Fig. 3. Left-to-write columns present comparative OCT-based and histological results for main molecular subtypes of IDC: low grade Luminal B (Her2/neo-) with fairly good treatment prognosis (orange box) and high grade invasive tumors with poor prognosis (grouped in big red box): Luminal B (Her2/neo +), non-luminal and triple-negative breast cancers. Magenta-color (solid line) rectangles in the CP OCT and OCE images indicate the areas covered by the respective histologic sections. The dashed-line rectangles in the OCE images indicate the tissue area over which histograms of the stiffness spectrum were calculated. Letters in the images indicated locations of agglomerates of tumor cells (TC), fibrous stroma (FS), hyalinized stroma (HS) and lymphocytic infiltrate (LI). Scale bars correspond to 0.5 mm in all panels. Unlike Fig. 1(e) the upper silicone layer is not shown in the OCE images.

The 1st and 2rd columns in Fig. 3 correspond to cancer subtypes Luminal B (Her2/neo-) and Luminal B(Her2/neo +), respectively. They have comparatively worse prognosis than Luminal A breast cancers and have higher histologic grade. Histologically these subtypes show that hyalinized tumor stroma is much stronger penetrated by densely packed tumor cells. This fact leads to significant increase in the stiffness for Luminal B tumors in comparison with Luminal A, which is clearly seen in histograms Figs. 3(q) and 3(r).

The 3rd and 4th columns in Fig. 3 correspond to the case of even more aggressive non-luminal and triple-negative breast cancers with high histologic grade and poor prognostic factors. The further pronounced shift of stiffness spectrum to even higher values for non-luminal and triple-negative breast cancer subtypes is consistent with the histologically confirmed significant disorganization of the collagen fibers' orientation and a significant increase in the tumor-cell area. Higher concentration of cancer cells in the tumor tissue leads to a more homogeneous distribution of high-stiffness areas in OCE-images Figs. 3(o) and 3(p) in comparison with Luminal B subtypes. It is worth to note that lymphocytic infiltration in the tumor that is distinguishable in histological slices for the triple-negative cancer, leads to somewhat decreased stiffness of the triple-negative breast cancers in comparison with the non-luminal subtype. Nevertheless, stiffness of the triple-negative breast cancer remains significantly higher than that of the hyalinized stroma.

Overall, consideration of the above-listed characteristic breast-tissue types confirmed that the OCT-based elastographic imaging looks very promising for distinguishing of different cancer subtypes with much higher contrast than it conventional and even polarization-sensitive structural OCT images. The 56 examined specimens (some of which are exemplified in Figs. 2 and 3) give clear evidence that there is a strong correlation between stromal and cellular tumor components diagnosed in histology and the distribution of stiffness in the OCE images. Examples similar to those in Fig. 3 show that in the case of high-grade breast cancer subtypes associated with poor treatment prognosis, the cancer zones demonstrate increased stiffness with fairly homogeneous spatial distribution. In the histological data this corresponds to a decrease in the content of the softer stromal component and predominance of stiffer regions of tumor cells. In the next section we discuss in more detail possibilities to quantify elastographic signatures of these tissue subtypes.

3.2. Quantitative processing of the OCE images

Detailed comparative examination of the OCE stiffness maps and the corresponding histological slices, for which tissue-type classification was made by an experienced histopathologist, made it possible to find the correspondence between several main breast-tissue components and corresponding ranges of their Young modulus.

Figure 4 shows the so-reconstructed distribution that can be called "stiffness spectra" for five characteristic breast-tissue components (adipose tissue, fibrous and hyalinized tumor stroma, lymphocytic infiltrate and agglomerates of tumor cells), including both normal and pathological states. To obtain each characteristic peak in the stiffness spectrum, 8-10 examples of the histologically confirmed localizations of the respective tissue component were examined. Figure 4 demonstrates that these tissue components are fairly well separated in terms of characteristic stiffness. Having such a reference stiffness ranges, stiffness maps for studied breast-tissue samples can be re-plotted in a form, in which the regions with the so-determined characteristic stiffness ranges are shown as color-coded localizations of the corresponding tissue components, i.e. the tissue morphology. Such segmentation of the initial stiffness map into zones corresponding to different tissue components is similar to delineation of morphological components based on examination of histological images (although the OCE maps have much lower resolution, ~40-50 μm in our examples). Certainly, there may be some overlapping and interpenetration of different tissue types, resulting in intermediate stiffness values. Nevertheless, morphological segmentation of stiffness maps may be rather

useful, especially in the zones of transitions with changing stiffness, for example, for clearer determining boundaries of invasive tumors with surrounding normal tissue.
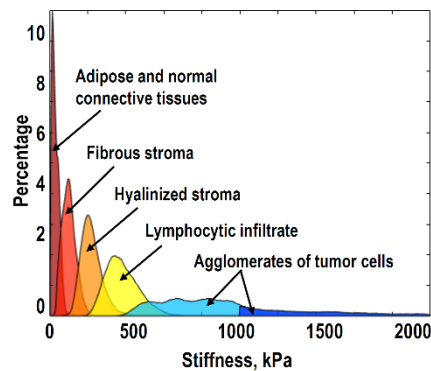

Fig. 4. Correspondence between the characteristic stiffness ranges and main types of breast-tissue components derived from detailed comparison of histological and OCE images.

Such an example is given in Fig. 5, where structural OCT images (in co- and cross polariazations), the corresponding histological slice, stiffness map and its morphological segmentation map (that is constructed using the stiffness spectrum shown in Fig. 4) are shown. The OCE-based stiffness map Fig. 5(c) and the derived OCE-based morphological segmentation image Fig. 5(d) demonstrate clear correspondence with the histological slice Fig. 5(b). The boundary between normal (peri-tumoral) tissue (left part of the images) and an invasive tumor (non-luminal subtype) is clearly seen in the histological image Fig. 5(b) and the stiffness map Fig. 5(c) and its segmented representation Fig. 5(d). In contrast, in the conventional structural OCT images in Fig. 5(a) there are no clear variations near the tumor boundary.
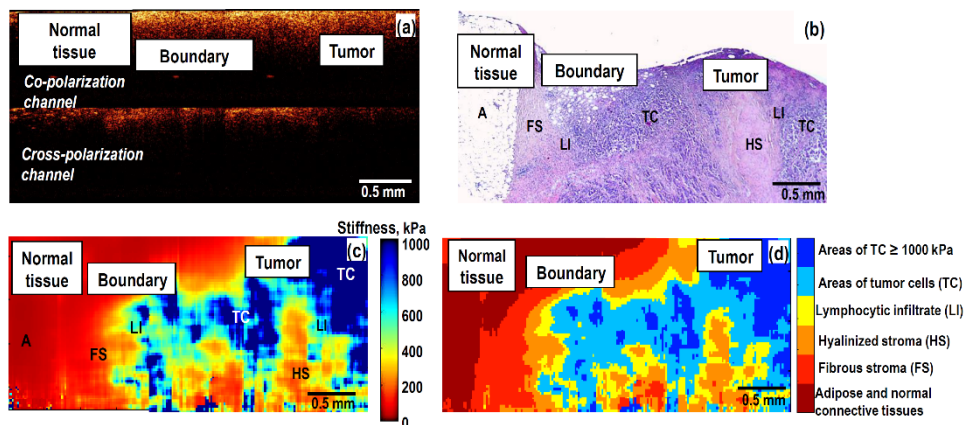

Fig. 5. Visualization of a transitional zone between peritumoral (normal) breast tissue and tumor region using structural CP OCT, histological image and OCE-based images: (a) is the CP OCT image; (b) is the H&E-histological slice; (c) is the stiffness map through approximately the same plane (we recall that after OCE examination the sample shape was noticeably distorted during preparation of the histological slices); (d) morphological segmentation of the OCE image into areas corresponding to various tissue components, for which stiffness ranges are shown in Fig. 4.

The next important point is whether OCE, in addition to visualization of the normal/cancer boundary and differentiation between low- and high-grade cancers like in Figs. 2 and 3, can be used for more fine classification. Especially important is differentiation

among non-invasive and invasive breast cancers of different molecular subtypes and histological grades. As a first step in this direction, Fig. 6 shows the most commonly used elastographic characteristic - average stiffness (E_{mean}) for the same eight breast-issue types that are shown in Figs. 2 and 3 (i.e., normal tissue and seven lesions). For each sample, E_{mean} corresponds to calculation of the mean Young modulus for individual stiffness histograms similar to those in Figs. 2 and 3. Then averaging is made for all samples of the same subtype.

The first observation is that the average stiffness shown in Fig. 6 demonstrates clear, statistically significant (p-value < 0.05) difference between the normal breast tissue stiffness (56 ± 16kPa) and the group of all other benign and malignant lesions (for which the mean stiffness ranges from 150 kPa to over 500 kPa).

Second, Fig. 6 shows that the benign and low-grade lesions shown in Fig. 2 above (fibroadenoma; non-invasive DCIS and invasive Luminal A breast cancer with E_{mean} ranging from 150 to 200 kPa in this group) demonstrate statistically significant (p < 0.05) difference from the three high-grade invasive cancer types. For the latter, E_{mean} is clearly higher than 400kPa: (Luminal B (Her2/neo +), non-luminal and triple-negative breast cancers (they were shown in columns 2,3 and 4 in Fig. 3 above).

However, the contrast in the mean stiffness among various tumor subtypes is significantly smaller than their difference from the normal tissue. Figure 6 also shows that the group of molecular subtype Luminal B (Her2/neo-) breast cancer has intermediate E_{mean} between the two groups of benign/low-grade and aggressive, high-grade invasive cancers. Standard deviations in the mean-stiffness values for these two groups overlap with the characteristic interval for Luminal B (Her2/neo-) breast cancer. Therefore, even if the difference in E_{mean} is statistically significant among the groups of breast cancer subtypes, evaluation of E_{mean} for individual samples is insufficient for identification of their subtype.
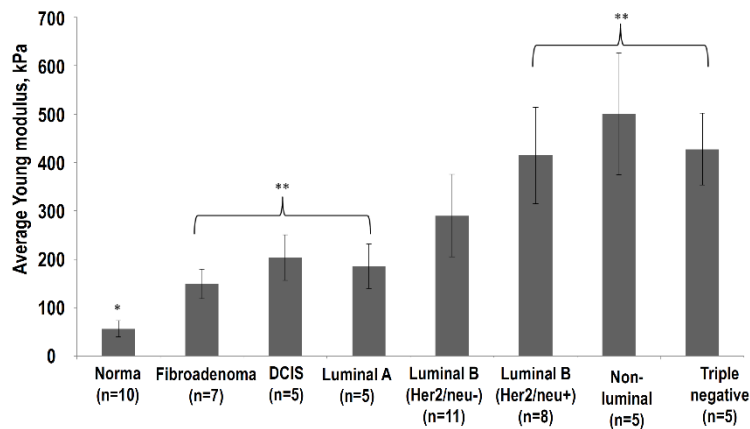

Fig. 6. Average Young modulus (E_{mean}) and standard deviation (SD) of stiffness for OCE images of breast cancer with different molecular subtypes. The E_{mean} were found for ROIs shown in Figs. 2 and 3. Asterisk (*) indicates a statistically significant difference between E_{mean} for normal breast tissue and all other molecular types of lesions (Bonferroni post-hoc test for multiple comparisons, with p < 0.05). Double asterisk (**) indicates a statistically significant difference (Bonferroni post-hoc test for multiple comparisons, with p < 0.05) between E_{mean} for breast lesions of low histological grade prognosis (fibroadenoma, DCIS, Luminal A) and 3 subtypes of the most-malignant (aggressive) invasive breast cancer with a poor prognosis (Luminal B (Her2/neo +), non-luminal and triple-negative); n is the number of examined samples for each subtype.

Another interesting observation is that, despite the average trend to stiffening with increasing histological grade of cancer, this trend is not strictly monotonic. Namely, in the low-grade group, more malignant invasive Luminal A subtype has somewhat smaller E_{mean} in comparison with the non-invasive DCIS subtype. A similar situation is in the group of high-

grade cancers, where the most malignant triple-negative breast cancer has E_{mean} smaller than the lower-grade non-luminal molecular subtype. Comparison with histological slices indicates that increased tissue stiffness is related to a larger concentration of tumor cells. In contrast, general reduction in stiffness of breast tumors is observed in areas with smaller concentrations of tumor cells, as well as partial atrophy of tumor cells penetrated in the surrounding (strongly hyalinized) stroma. Such processes may explain the fact that for non-invasive DCIS localized inside ducts, E_{mean} may be greater than for invasive Luminal A breast cancer, for which tumor cells migrate through the surrounding stroma.

Overall, Fig. 6 indicates that variability of E_{mean} for individual samples may be even stronger than the difference among various lesion types with different morphology, even if the inter-group difference in E_{mean} is statistically significant. In view of this and bearing in mind that main tissue components have significantly different stiffness (see Fig. 4), it is reasonable to consider in more detail percentage of pixels with different ranges of the Young modulus (normalized stiffness spectrum), as well as spatial features in OCE images.

The summary of such stiffness spectra showing percentage of different tissue components (identified as characteristic stiffness ranges) is presented in Fig. 7 for the same seven lesion subtypes and non-tumor samples as in Fig. 6. The characteristic stiffness ranges are chosen in agreement with the stiffness spectrum for the main tissue components shown in Fig. 4. In comparison with a single average modulus shown in Fig. 6, such stiffness distributions give more detailed representation about the difference between various lesion subtypes. The processing ROI (that are shown in Figs. 2 and 3) are the same for Figs. 6 and 7.
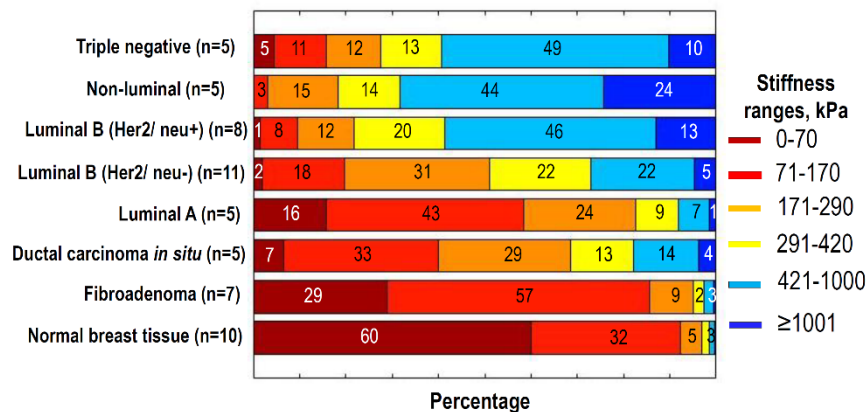

Fig. 7. Percentage of pixels belonging to different stiffness ranges (normalized stiffness spectrum) for normal tissue, fibroadenoma, DCIS and 5 invasive breast cancer with different molecular subtypes the same as in Fig. 6 (for each group the number *n* of examined samples is given in the parenthes). The spectra were found for ROI shown in Figs. 2 and 3. To give a better impression about similarity/variability of elastic properties of individual specimens, "Appendix A1" demonstrates stiffness spectra for individual samples from the following 3 groups: Luminal B (Her2/neu +), Luminal B (Her2/neu-) and fibroadenoma. Besides, "Appendix A2" presents several examples of differently chosen ROI windows for the same sample (Non-luminal cancer) to illustrate robustness of the normalized spectra to variations in the ROI position and size.

The upper three types of the most malignant breast cancers in Fig. 7, in agreement with Fig. 6, have much greater content of components with high stiffness >420 kPa. For non-luminal (Her2/neu +) subtype, in addition to overall increased content of the high-stiffness components, especially increased proportion (~2 times) of very stiff regions (>1000 kPa) can be noted, which differs it from both triple-negative and Luminal B (Her2/neu +) subtypes of breast cancer. The latter two types do not strongly differ from each other by the total content of stiffer fractions (>420 kPa), but the softest-fraction content is pronouncedly (~5 times) greater for triple-negative than for Luminal B (Her2/neu +) breast cancer.

The intermediate-grade Luminal B (Her2/neu-) breast cancer was not clearly distinguishable from both lower-grade and higher-grade types in terms of their average stiffness values shown in Fig. 6. In Fig. 7 the contrast for Luminal B (Her2/neu-) cancer in terms of the stiffness spectra looks significantly higher. Especially strong is the difference in the stiffer-component content: ~1.5-2 times lower than for higher-grade cancers and ~1.5-2 times higher than in lower-grade ones.

At the 4 lower rows in Fig. 7 comprising non-tumor tissue and 3 subtypes of low-grade lesions, the normal tissue has also pronouncedly different stiffness spectrum from all other types, especially in the percentage of the softest component with stiffness <70 кПа. In comparison with norm, fibroadenoma has significantly smaller (~2 times) percentage of the softest component (but 2-4 greater in comparison with DCIS and Luminal A breast cancers). In contrast to the malignant lesions (DSIC and Luminal A) from the low-grade group, fibroadenoma has the largest (over 1.5 times greater) percentage of the fibrous stroma with stiffness in the range 70-170 kPa, but pronouncedly (>2-3 times) smaller content of hyalinized stroma (170-290 kPa) and even smaller content of the stiffest (>290kPa) components in comparison with malignant low-grade lesions. Although in the content of fibrous component (70-100kPa) fibroadenoma and Luminal A cancer does not differ strongly, for the percentage of the softest and stiffest components, the contrast is much higher. Namely, fibroadenoma has ~2 times larger percentage of the softest adipose and ~3 times smaller percentage of the stiffest (>290kPa) component than Luminal A cancer. This once again demonstrates that for the compared lesion types, the contrast in terms of specific stiffness ranges may be significantly greater than hardly distinguishable difference in the mean stiffness shown in Fig. 6.

Concerning DCIS and Luminal A subtypes of breast cancer that have almost coinciding mean stiffness in Fig. 6, the percentage diagrams in Fig. 7 also show much stronger difference between these two lesions. Namely, although the content of intermediate-stiffness fractions in these subtypes does not strongly differ, the content of the softest adipose (<70 kPa) component in DCIS is over 2 times smaller, whereas the most stiff (>420kPa) component content is ~3 times greater in comparison with Luminal A breast cancer.

The difference in spatial localization of stiff regions in elastographic maps for low-grade (Fig. 2) and high-grade lesions (Fig. 3) can additionally be useful for differentiation between the two main groups of low- and higher-grade cancer subtypes. Then more detailed examination of stiffness spectra shown in Fig. 7 for 8 tissue types can be used to differentiate subtypes within each of the two groups of low-grade and high-grade tumors.

In this study we limit ourselves to the above-presented preliminary discussion of the revealed contrast in terms of stiffness spectra for various types of cancer. Certainly, further accumulation of OCE data and rigorous statistical analysis are required to verify the diagnostic value of the above presented encouraging results based on examination of a set of 56 samples comprising 7 subtypes of lesions. However, even these yet limited data demonstrate that, in addition to conventionally discussed mean stiffness values, analysis of the OCE-based stiffness spectra opens very promising prospects for distinguishing low-grade and high-grade tumors and even for finer differentiation of subtypes within those groups.

4. Discussion and conclusions

In the above sections we demonstrated that OCE imaging ensures much higher contrast between different tissue types in comparison with both structural OCT images (including polarization-sensitive ones) and conventionally used elastographic techniques, e.g. ultrasound-based ones. The latter have proven to be sufficient for approximate localization of tumor and discrimination between benign and malignant breast lesions [29,30]. However, more precise cancer margin detection that could be feasible intraoperatively and, moreover, intraoperative differentiation between various malignant cancers subtypes remains challenging [20].

The above-presented OCE-based results open promising prospects for solving these clinically very important and challenging problems. The above described OCE procedures and subsequent drawing of conclusions about the margin positions and tissue subtypes may be performed on a scale of minutes without special preparation of the tissue samples and, therefore, can be feasible intra-operatively.

We emphasize that during OCE examinations, by analogy with sample scales in conventional biopsy procedures, the classification of lesions was made by analyzing in-depth B-scans with 2-4 mm lateral size and ~1 mm in depth. However, the freshly-excised tissue samples did not require special preparation for obtaining OCE images. Such OCE B-scans could be readily obtained on time intervals ~minute and repeated for several positions/orientations without special preparation procedures. Even in such a form this may already be helpful in assessment of clean tumor boundary in organ-conserving surgical operations. The application of more advanced OCT systems with wider field of view and much faster acquisition rate would allow for realization of the proposed OCE-assessment and tumor delineation even in 3D.

The above-described procedures can be viewed as a kind of OCE-based optical biopsy in view of similarity in the examined sample sizes with conventional biopsies (e.g., obtained by biopsy forceps). The richness of the extracted information from OCE examination may be comparable with histology, although the resolution of OCE-scans ~40-50 μm is lower than in microscopic histological studies.

The developed OCE procedures with resolution/detailing unavailable to conventional elastographic techniques demonstrate a good agreement with histological conclusions about the morphology of the specimens and even reveal correlation with molecular portraits of the samples. Certainly, exact determining of molecular subtypes of tumors requires immuno-histochemical analysis of the samples. Such procedures are expensive, laborious and very time-consuming in comparison with the proposed express OCE-assessment of breast-cancer tissues (potentially intraoperatively feasible). Thus, the revealed interrelation between the molecular status of tumors with their morphological and biomechanical properties looks very encouraging. In this context, one can mention an analogy with ultrasound-based determining of protein and lipid content in blood serum, which is successfully used in commercially available devices [31]. This ultrasonic method (that is much faster and cheaper than conventional biochemical procedures) is based on empirically established relationships between the protein/lipid concentrations in blood serum and its biomechanical parameters that affect the measured resonant properties of a small cavity filled with the analyzed liquid. Concerning specifically breast-cancer samples, our results are supported by recent independent data about the existence of interrelation between the molecular status of tumors and their morphology [32,33]. Studies [34,35] revealed correlation of immunohistochemistry results with the data on morphology of tumors in combination with the results of conventional ultrasound elastography and histological images.

The proposed OCE-based examination/classification procedures open prospects for doctors to rapidly (even intra-operatively) assess the tissue state and stage of the lesion development. Indeed, based on the tissue type - fibrosis, hyalinosis, inflammation, tumor-cell agglomerates (clearly distinguishable in OCE scans) - the surgeon can conclude how long the tumor has been developed and how aggressive it is. This understanding is important for choosing the surgery type: either radical resection (mastectomy) or organ-preserving lumpectomy, for which clean tumor margin detection may also be intraoperatively guided by OCE examination. Besides, the rapidly feasible OCE-based assessment/classification (e.g., discrimination between triple-negative and Luminal A or B subtypes of breast cancer) can be a useful guidance for recommendations on post-operation treatment, because these cancer types require significantly different types of chemotherapy.

Further accumulation of statistics is required for better understanding of the diagnostic accuracy of the proposed OCE-based procedures, their optimization and development of

automated analysis. However, even at the present stage with manual ROI selection, the proposed OCE procedures have demonstrated very encouraging prospects for rapid and easily feasible discrimination between the groups of high- and low-grade lesions (grouped in Figs. 2 and 3, respectively). The proposed OCE-based biopsy procedures do not require special sample preparation (fixation, dehydration, staining, etc.) and can readily be combined with other OCT-based methods for tumor/no-tumor discrimination, such as polarization-sensitive OCT [10,11] or methods based on scan-texture analysis [36]. Afterwards, the same tissue sample can be used for conventional histological/immuno-histochemical studies that are much more time consuming.

The richness of the extracted information (including segmentation of OCE maps reflecting sample morphology like in Fig. 5(d) with detalization ~tens micron, differentiation of low-grade and high-grade cancer groups and even more detailed discrimination of cancer subtypes within those groups) gives reasons to consider the proposed procedures as a kind of express OCE-based optical biopsy with potential of intraoperative application.

Appendix

A1. Illustration of similarity/variability of individual stiffness-range graphs for specimens of the same lesion type determined by histo-chemical analysis

The below examples are given for three series of samples of the same lesion type (fibroadenoma, Luminal B (Her2/neu-) and Luminal B (Her2/neu+), for which the number of samples was larger than for other lesion types. These examples give a representation about variability of individual stiffness spectra for samples of the same subtype.
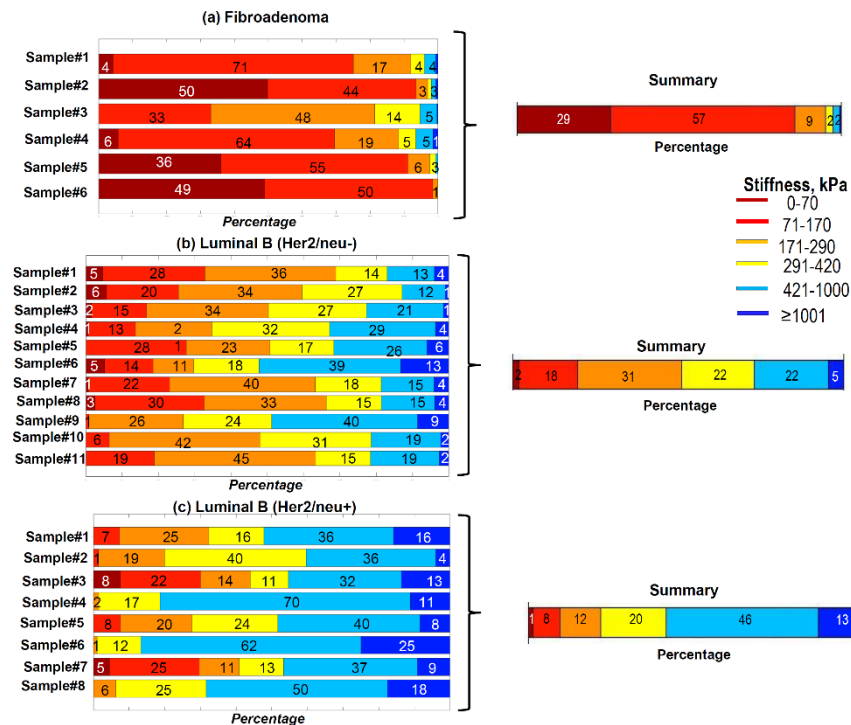

Fig. 8. Stiffness-percentage graphs for individual tumor specimens of the same type. The right half of the figure shows the resultant averaged graphs the same as in Fig. 7.

Despite the individual variability, distinctions between the compared groups are significantly more pronounced in terms of stiffness spectra and stiffness-percentage graphs in comparison with estimates of the mean Young modulus.

Preliminary considerations of the "distances" (e.g., conventional Euclidian ones) between the compared groups in the 6D space were made by considering the percentages of pixels belonging to the 6 characteristic stiffness ranges as 6D vectors. Such comparisons of distances between the averaged percentage vector for a suspected lesion subtype and percentage vectors for individual samples can be automated and used for classification of the samples. For example, among 11 samples of Luminal B (Her2/neu-) shown in panel (b) in Fig. 8 the 9 samples correctly demonstrated closer distances to the averaged stiffness vector for Luminal B (Her2/neu-) subtype. Only Luminal B (Her2/neu-) samples #6 and #9 demonstrated closer distances to the averaged vector for Luminal B (Her2/neu+) subtype. This means that 81% of the Luminal B (Her2/neu-) were correctly classified.

A2. Illustration of robustness of the normalized stiffness histograms and the corresponding stiffness-percentage graphs with respect to the ROI-window choice

The following example illustrates how the choice of ROI-window size and position affect the calculated stiffness spectrum. Figure 9 demonstrates that despite significantly differing positions and sizes of the ROI windows shown in the figure, there is a pronounced similarity in the normalized stiffness histograms and in the corresponding stiffness-percentage graphs for all 4 positions and sizes of the ROI windows.
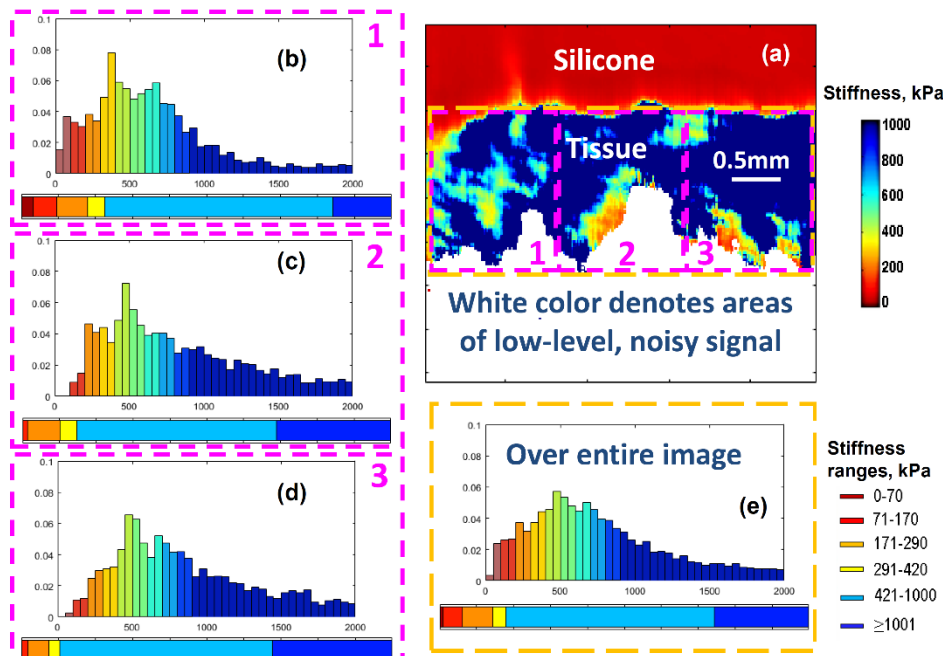

Fig. 9. Illustration of the dependence of the calculated stiffness spectrum on the size and position of the ROI window. Panel (a) is the stiffness map for one of specimens of invasive Non-luminal cancer similar to OCE maps shown in Figs. 2 and 3, but shown together with the silicone layer. The dashed rectangles (magenta color) labeled 1,2, and 3 show the ROI zones covering 1/3 of the OCE image area. The histograms (b), (c) and (d) labeled by the corresponding numbers show the stiffness spectra for each of the 3 ROI windows. The histogram (e) is calculated for the larger ROI window shown by the yellow dashed rectangle in panel (a). The color-ribbons below the histograms are the stiffness-percentage graphs similar to those in Fig. 7 corresponding to the smaller ROI windows from 1 to 3 in panels (b), (c) and (d) and the larger ROI window over the entire OCE scan of the tissue stiffness (panel (e)).

On the stiffness map, the areas of low-level and, therefore, noisy signal in the initial structural images were excluded by applying the amplitude thresholding to the recorded OCT scans. The excluded areas are shown by white color in Fig. 9(a).

These examples illustrate that if the ROI-window is not too small to ensure that in average the stiffness map is fairly homogeneous within the chosen window, the resultant stiffness spectra do not strongly depend on the ROI-window choice. Empirically it was found that the lateral size of the window ~ 1-2 mm usually is sufficient for obtaining such fairly robust stiffness spectra. The presence of pronounced transitions in OCE maps (like in Fig. 5) is easily seen in the OCE-images. Consequently, the ROI-windows covering more homogeneous parts of the image can be chosen to compare the stiffness spectra for different sub-regions in such cases.

Funding

Acknowledgments

Disclosures

The authors declare that there are no conflicts of interest related to this article.

References

1. R. L. Siegel, K. D. Miller, and A. Jemal, "Cancer statistics, 2018," CA Cancer J. Clin. **68**(1), 7–30 (2018).
2. M. A. Aleskandarany, M. E. Vandenberghe, C. Marchiò, I. O. Ellis, A. Sapino, and E. A. Rakha, "Tumour Heterogeneity of Breast Cancer: From Morphology to Personalised Medicine," Pathobiology **85**(1-2), 23–34 (2018).
3. K. Iwao, R. Matoba, N. Ueno, A. Ando, Y. Miyoshi, K. Matsubara, S. Noguchi, and K. Kato, "Molecular classification of primary breast tumors possessing distinct prognostic properties," Hum. Mol. Genet. **11**(2), 199–206 (2002).
4. K. H. Allison, "Molecular pathology of breast cancer: what a pathologist needs to know," Am. J. Clin. Pathol. **138**(6), 770–780 (2012).
5. M. S. Moran, S. J. Schnitt, A. E. Giuliano, J. R. Harris, S. A. Khan, J. Horton, S. Klimberg, M. Chavez-MacGregor, G. Freedman, N. Houssami, P. L. Johnson, and M. Morrow, "Society of Surgical Oncology-American Society for Radiation Oncology consensus guideline on margins for breast-conserving surgery with whole-breast irradiation in stages I and II invasive breast cancer," Int. J. Radiat. Oncol. Biol. Phys. **88**(3), 553–564 (2014).
6. A. Luini, J. Rososchansky, G. Gatti, S. Zurrida, P. Caldarella, G. Viale, G. Rosali dos Santos, and A. Frasson, "The surgical margin status after breast-conserving surgery: discussion of an open issue," Breast Cancer Res. Treat. **113**(2), 397–402 (2009).
7. O. A. Catalano, G. L. Horn, A. Signore, C. Iannace, M. Lepore, M. Vangel, A. Luongo, M. Catalano, C. Lehman, M. Salvatore, A. Soricelli, C. Catana, U. Mahmood, and B. R. Rosen, "PET/MR in invasive ductal breast cancer: correlation between imaging markers and histological phenotype," Br. J. Cancer **116**(7), 893–902 (2017).
8. F. T. Nguyen, A. M. Zysk, E. J. Chaney, J. G. Kotynek, U. J. Oliphant, F. J. Bellafiore, K. M. Rowland, P. A. Johnson, and S. A. Boppart, "Intraoperative evaluation of breast tumor margins with optical coherence tomography," Cancer Res. **69**(22), 8790–8796 (2009).
9. X. Yao, Y. Gan, E. Chang, H. Hibshoosh, S. Feldman, and C. Hendon, "Visualization and tissue classification of human breast cancer images using ultrahigh-resolution OCT," Lasers Surg. Med. **49**(3), 258–269 (2017).
10. F. A. South, E. J. Chaney, M. Marjanovic, S. G. Adie, and S. A. Boppart, "Differentiation of ex vivo human breast tissue using polarization-sensitive optical coherence tomography," Biomed. Opt. Express **5**(10), 3417–3426 (2014).
11. R. Patel, A. Khan, R. Quinlan, and A. N. Yaroslavsky, "Polarization-sensitive multimodal imaging for detecting breast cancer," Cancer Res. **74**(17), 4685–4693 (2014).
12. K. J. Parker, M. M. Doyley, and D. J. Rubens, "Imaging the elastic properties of tissue: the 20 year perspective," Phys. Med. Biol. **56**(1), R1–R29 (2011).
13. B. F. Kennedy, S. H. Koh, R. A. McLaughlin, K. M. Kennedy, P. R. Munro, and D. D. Sampson, "Strain estimation in phase-sensitive optical coherence elastography," Biomed. Opt. Express **3**(8), 1865–1879 (2012).

14. K. M. Kennedy, L. Chin, R. A. McLaughlin, B. Latham, C. M. Saunders, D. D. Sampson, and B. F. Kennedy, "Quantitative micro-elastography: imaging of tissue elasticity using compression optical coherence elastography," Sci. Rep. **5**(1), 15538 (2015).

15. V. Y. Zaitsev, A. L. Matveyev, L. A. Matveev, G. V. Gelikonov, A. A. Sovetsky, and A. Vitkin, "Optimized phase gradient measurements and phase-amplitude interplay in optical coherence elastography," J. Biomed. Opt. **21**(11), 116005 (2016).

16. V. Y. Zaitsev, A. L. Matveyev, L. A. Matveev, E. V. Gubarkova, A. A. Sovetsky, M. A. Sirotkina, G. V. Gelikonov, E. V. Zagaynova, N. D. Gladkova, and A. Vitkin, "Practical obstacles and their mitigation strategies in compressional optical coherence elastography of biological tissues," J. Innov. Opt. Health Sci. **10**(06), 1742006 (2017).

17. B. F. Kennedy, R. A. McLaughlin, K. M. Kennedy, L. Chin, P. Wijesinghe, A. Curatolo, A. Tien, M. Ronald, B. Latham, C. M. Saunders, and D. D. Sampson, "Investigation of Optical Coherence Microelastography as a Method to Visualize Cancers in Human Breast Tissue," Cancer Res. **75**(16), 3236–3245 (2015).

18. W. M. Allen, L. Chin, P. Wijesinghe, R. W. Kirk, B. Latham, D. D. Sampson, C. M. Saunders, and B. F. Kennedy, "Wide-field optical coherence micro-elastography for intraoperative assessment of human breast cancer margins," Biomed. Opt. Express **7**(10), 4139–4153 (2016).

19. L. Chin, B. Latham, C. M. Saunders, D. D. Sampson, and B. F. Kennedy, "Simplifying the assessment of human breast cancer by mapping a micro-scale heterogeneity index in optical coherence elastography," J. Biophotonics **10**(5), 690–700 (2017).

20. B. W. Maloney, D. M. McClatchy, B. W. Pogue, K. D. Paulsen, W. A. Wells, and R. J. Barth, "Review of methods for intraoperative margin detection for breast conserving surgery," J. Biomed. Opt. **23**(10), 1–19 (2018).

21. A. A. Moiseev, G. V. Gelikonov, D. A. Terpelov, P. A. Shilyagin, and V. M. Gelikonov, "Noniterative method of reconstruction optical coherence tomography images with improved lateral resolution in semitransparent media," Laser Phys. Lett. **10**(12), 125601 (2013).

22. V. M. Gelikonov and G. V. Gelikonov, "New approach to crosspolarized optical coherence tomography based on orthogonal arbitrarily polarized modes," Laser Phys. Lett. **3**(9), 445–451 (2006).

23. V. M. Gelikonov, V. N. Romashov, D. V. Shabanov, S. Y. Ksenofontov, D. A. Terpelov, P. A. Shilyagin, G. V. Gelikonov, and I. A. Vitkin, "Cross-polarization optical coherence tomography with active maintenance of the circular polarization of a sounding wave in a common path system," Radiophys. Quantum Electron. **60**(11), 897–911 (2018).

24. A. A. Sovetsky, A. L. Matveyev, L. A. Matveev, D. V. Shabanov, and V. Y. Zaitsev, "Manually-operated compressional optical coherence elastography with effective aperiodic averaging: demonstrations for corneal and cartilaginous tissues," Laser Phys. Lett. **15**(8), 085602 (2018).

25. A. L. Matveyev, L. A. Matveev, A. A. Sovetsky, G. V. Gelikonov, A. A. Moiseev, and V. Y. Zaitsev, "Vector method for strain estimation in phase-sensitive optical coherence elastography," Laser Phys. Lett. **15**(6), 065603 (2018).

26. V. Y. Zaitsev, A. L. Matveyev, L. A. Matveev, G. V. Gelikonov, E. V. Gubarkova, N. D. Gladkova, and A. Vitkin, "Hybrid method of strain estimation in optical coherence elastography using combined sub-wavelength phase measurements and supra-pixel displacement tracking," J. Biophotonics **9**(5), 499–509 (2016).

27. T. A. Krouskop, T. M. Wheeler, F. Kallel, B. S. Garra, and T. Hall, "Elastic moduli of breast and prostate tissues under compression," Ultrason. Imaging **20**(4), 260–274 (1998).

28. A. A. Plekhanov, M. A. Sirotkina, A. A. Sovetsky, E. V. Gubarkova, E. B. Kiseleva, V. Y. Zaitsev, L. A. Matveev, A. L. Matveyev, S. S. Kuznetsov, E. V. Zagaynova, and N. D. Gladkova, "Optical coherence elastography as a new method for estimation of chemotherapy efficacy on triple-negative breast cancer in the experiment " Proc SPIE International Symposium on Optics and Biophotonics VI: Saratov Fall Meeting 2018 **15**, 1–8, in print (2019).

29. J. Tian, Q. Liu, X. Wang, P. Xing, Z. Yang, and C. Wu, "Application of 3D and 2D quantitative shear wave elastography (SWE) to differentiate between benign and malignant breast masses," Sci. Rep. **7**(1), 41216 (2017).

30. J. M. Chang, W. K. Moon, N. Cho, A. Yi, H. R. Koo, W. Han, D. Y. Noh, H. G. Moon, and S. J. Kim, "Clinical application of shear wave elastography (SWE) in the diagnosis of benign and malignant breast diseases," Breast Cancer Res. Treat. **129**(1), 89–97 (2011).

31. S. N. Gurbatov, I. Y. Demin, A. V. Klemina, and V. A. Klemin, "Acoustic Analysis of the Composition of Human Blood Serum," Acoust. Phys. **55**(4-5), 510–518 (2009).

32. M. Boisserie-Lacroix, G. Hurtevent-Labrot, S. Ferron, N. Lippa, H. Bonnefoi, and G. Mac Grogan, "Correlation between imaging and molecular classification of breast cancers," Diagn. Interv. Imaging **94**(11), 1069–1080 (2013).

33. S. Tiwari, R. Malik, V. K. Trichal, R. K. Nigam, A. Rai, S. Balani, J. Jain, and D. Pandey, "Breast Cancer: Correlation of Molecular Classification with Clinicohistopathology," Sch. J. App. Med. Sci. **3**, 1018–1026 (2015).

34. V. E. Gazhonova, M. P. Efremova, and E. A. Dorokhova, "Correlation between US-imaging with use of 3D ABWS and immune-histochemical profile of breast cancer invasive carcinomas [in Russian]," Oncology bulletin of the Volga region **2**, 26–32 (2016).

35. J. M. Chang, I. A. Park, S. H. Lee, W. H. Kim, M. S. Bae, H. R. Koo, A. Yi, S. J. Kim, N. Cho, and W. K. Moon, "Stiffness of tumours measured by shear-wave elastography correlated with subtypes of breast cancer," Eur. Radiol. **23**(9), 2450–2458 (2013).

36. A. Moiseev, L. Snopova, S. Kuznetsov, N. Buyanova, V. Elagin, M. Sirotkina, E. Kiseleva, L. Matveev, V. Zaitsev, F. Feldchtein, E. Zagaynova, V. Gelikonov, N. Gladkova, A. Vitkin, and G. Gelikonov, "Pixel classification method in optical coherence tomography for tumor segmentation and its complementary usage with OCT microangiography," J. Biophotonics **11**(4), e201700072 (2018).